

See discussions, stats, and author profiles for this publication at: <https://www.researchgate.net/publication/11212356>

# A Chaotic Electroosmotic Stirrer

ARTICLE *in* ANALYTICAL CHEMISTRY · SEPTEMBER 2002

Impact Factor: 5.64 · DOI: 10.1021/ac025601i · Source: PubMed

---

CITATIONS

111

---

READS

46

## 2 AUTHORS:



Shizhi Qian

Old Dominion University

155 PUBLICATIONS 2,495 CITATIONS

SEE PROFILE



Haim H Bau

University of Pennsylvania

259 PUBLICATIONS 6,414 CITATIONS

SEE PROFILE

# A Chaotic Electroosmotic Stirrer

Shizhi Qian and Haim H. Bau\*

Department of Mechanical Engineering and Applied Mechanics, University of Pennsylvania, Philadelphia, Pennsylvania 19104-6315

**Two-dimensional, time-independent, and time-dependent electroosmotic flows driven by a uniform electric field in a conduit with nonuniform  $\zeta$  potential distributions along its walls are investigated theoretically. The time-independent flow fields are computed with the aid of Fourier series. The series' convergence is accelerated so that highly accurate solutions are obtained with just a few terms in the series. The analytic solution is used to compute flow patterns for various distributions of the  $\zeta$  potential along the conduit's boundaries. Subsequently, it is demonstrated that by time-wise periodic alternations of the  $\zeta$  potentials, one can induce chaotic advection. This chaotic flow can be used to efficiently stir and mix fluids in microfluidic devices.**

In recent years, there has been a growing interest in developing microfluidic systems for biological and chemical minute "laboratories on a chip".<sup>1–3</sup> Often it is necessary to propel fluids from one part of the device to another, control fluid motion, enhance mixing, and separate fluids. Electroosmosis provides an attractive means for manipulating liquids in microdevices. The electroosmotic phenomenon is caused by the accumulation of net electric charge on the solid's surface that is in contact with an electrolyte solution and the presence of counterions accumulated in a thin liquid (double or Debye) layer next to the solid's surface. Away from the solid's surface, the electrolyte is neutral. This charge separation next to the solid wall causes either a positive or negative ( $\zeta$ ) potential difference across the Debye layer. In the presence of an external electric field, the counterions in the Debye layer are attracted to the oppositely charged electrode and drag the liquid along. In other words, the electric field, through its effect on the counterions, creates a body force that, in turn, induces fluid motion. In many cases, the Debye layer thickness is much smaller than the conduit's dimensions, and the electroosmotic flow can be studied by specifying a "slip velocity" at the wall.

Most of the studies to date have focused on electroosmotic flows in straight conduits with uniform  $\zeta$  potentials along the conduits' walls. See, for example, Dutta and Beskok<sup>4</sup> and the references therein. Recently, however, Ajdari<sup>5–7</sup> studied complex electroosmotic flows induced by nonuniform, time-independent,

and time-dependent  $\zeta$  potentials along the conduits' walls. Non-uniform  $\zeta$  potentials can be obtained by coating the conduits' walls with different materials<sup>8</sup> or by using different buffer solutions. Both spatial and temporal control of the  $\zeta$  potential can be achieved by imposing an electric field perpendicular to the solid–liquid interface.<sup>9–12</sup> Such normal electric fields can be imposed with the aid of electrodes embedded beneath the solid–liquid interface and electrically insulated from the liquid. Alternatively, when the solid's surface is photosensitive (such as a semiconducting TiO<sub>2</sub> film), the surface charge can be modified with light.<sup>13</sup>

In this paper, we study electroosmotic flows in conduits with nonuniform  $\zeta$  potentials along the conduits' walls, and we demonstrate that by temporal modulation of the  $\zeta$  potential, it is possible to induce chaotic advection. The paper is organized as follows: after setting up the mathematical model, we use slip boundary conditions at the walls and solve the Stokes equation to obtain two-dimensional electroosmotic flows for various distributions of the  $\zeta$  potential. Since later in the paper we require highly accurate and compact expressions for the velocity field in order to track passive tracer particles, we determine the flow field analytically using Fourier series. By studying the asymptotic behavior of the series' coefficients, we are able to overcome the usual shortcoming of the Fourier series (slow convergence) and accelerate their rate of convergence so that just a few terms are needed to obtain highly accurate solutions. Finally, following ideas promoted by Aref,<sup>14</sup> we alternate periodically between two different flow fields and demonstrate that one can induce chaotic advection in the conduit. Such modulation can be implemented by embedding electrodes beneath the solid–liquid interface<sup>9–12</sup> and periodically alternating the electrodes' potentials. The ability of such chaotic flows to stir the fluid is demonstrated by following the advection of passive tracer particles. Similar methods can be used to achieve efficient stirring in microdevices.

## MATHEMATICAL MODEL

Consider the two-dimensional conduit of height  $2H$  depicted in Figure 1. The Cartesian coordinates  $x$  and  $y$  ( $|y| \leq H$ ) are,

- (8) Stroock, A. D.; Weck, M.; Chiu, D. T.; Huck, W. T. S.; Kenis, P. J. A.; Ismagilov, R. F.; Whitesides, G. M. *Phys. Rev. Lett.* **2000**, *84*, 3314–3317.
- (9) Lee, C. S.; Blanchard, W. C.; Wu, C.-T. *Anal. Chem.* **1990**, *58*, 1550–1552.
- (10) Hayes, M. A.; Ewing, A. G. *Anal. Chem.* **1992**, *64*, 512–516.
- (11) Schasfoort, R. B. M.; Schlautmann, S.; Hendrikse, J.; Van den Berg, A. *Science* **1999**, *286*, 942–945.
- (12) Buch, J. S.; Wang, P.-C.; DeVoe, D. L.; Lee, C. S. *Electrophoresis* **2001**, *22*, 3902–3907.
- (13) Moorthy, J.; Khoury, C.; Moore, J. S.; Beebe, D. J. *Sens. Actuators B* **2001**, *75*, 223–229.
- (14) Aref, H. J. *Fluid Mech.* **1984**, *143*, 1–21.

\* To whom correspondence should be addressed. E-mail: bau@seas.upenn.edu.

(1) Jensen, K. F. *AIChE J.* **1999**, *45*, 2051–2054.

(2) Langer, R. *AIChE J.* **2000**, *46*, 1286–1289.

(3) Stone, H. A.; Kim, S. *AIChE J.* **2001**, *47*, 1250–1254.

(4) Dutta, P.; Beskok, A. *Anal. Chem.* **2001**, *73*, 1979–1986.

(5) Ajdari, A. *Phys. Rev. Lett.* **1995**, *75*, 755–758.

(6) Ajdari, A. *Phys. Rev. E* **1996**, *53*, 4996–5005.

(7) Ajdari, A. *Phys. Rev. E* **2000**, *61*, R45–R48.

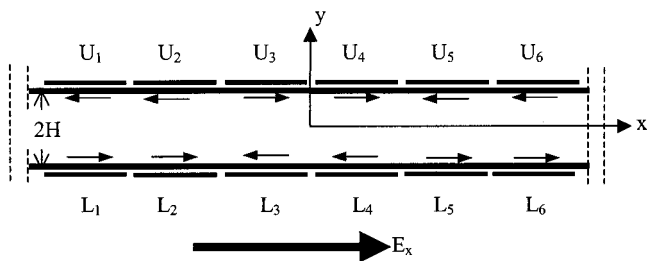


Figure 1. Conduit equipped with electrodes ( $U_i$ ) and ( $L_i$ ) embedded, respectively, in the upper and lower walls. These electrodes are used to control the  $\zeta$  potential at the solid/liquid interface. The arrows in the channel denote the directions of the electroosmotic velocities that were used to generate flow pattern A.

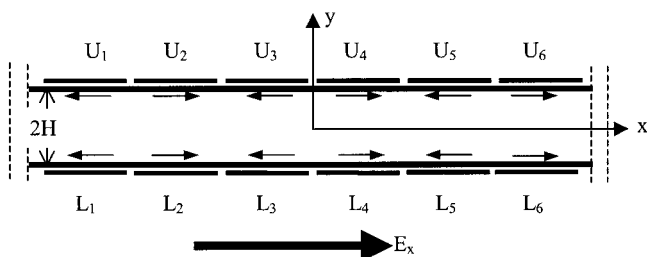


Figure 2. By judicious control of the embedded electrodes, one can control the  $\zeta$  potential distribution. The arrows denote the directions of the electroosmotic velocities that were used to generate flow pattern B.

respectively, aligned along the conduit's axis and in a direction that is perpendicular to the conduit's walls. The channel is filled with a weak electrolyte solution that is subjected to a uniform electric field,  $E_x$ , that is parallel to the  $x$  axis. As a result of the interaction of the ionized solution with static charges on the solid walls, a thin electric double layer (EDL) of thickness  $\lambda_D$  forms next to the solid walls.<sup>15</sup> The EDL contains an excess of counterions. The electrostatic forces generated by the external electric field ( $E_x$ ) induce fluid motion. Since typically,  $\lambda_D \ll H$ , the liquid motion can be adequately described by specifying the Helmholtz–Smoluchowski slip (electroosmotic) velocity,<sup>4,15,16</sup>  $-\epsilon E_x(\zeta^*)/\mu$ , next to the solid walls. In the above,  $\zeta^*$  is the dimensional  $\zeta$  potential,  $\mu$  is the liquid's viscosity, and  $\epsilon$  is the liquid's dielectric constant. One can control the magnitude and the direction of the electroosmotic velocity by controlling the magnitude and sign of the  $\zeta$  potential. One convenient method of controlling the  $\zeta$  potential is by imposing electric fields normal to the solid–liquid interface. Such electric fields can be produced with the aid of individually controlled electrodes embedded beneath the solid's surface.<sup>9–12</sup> Figures 1 and 2 describe schematically one such arrangement. The electrodes embedded in the conduit's upper and lower walls are labeled, respectively, with the letters ( $U_i$ ) and ( $L_i$ ). The arrows in Figures 1 and 2 indicate the direction of the electroosmotic velocity as dictated by the control electrodes' potentials. Clearly, by appropriate specification of the electrodes' potentials, one can induce complex flows in the conduit. Ajdari<sup>5–7</sup> studied theoretically and experimentally such time-independent complex flows. Their theoretical models assumed highly idealized, harmonic distributions of the  $\zeta$  potential. In this section, we study

a less idealized model that assumes nonuniform  $\zeta$  potentials along finite length segments of the walls. In the following sections, we will demonstrate that with time modulation of the  $\zeta$  potential, one can induce chaotic advection.

We model the flow with the dimensionless Stokes equation.<sup>16</sup>

$$Re \frac{\partial \vec{V}}{\partial t} = -\nabla p + \nabla^2 \vec{V} \quad (2.1)$$

In the above,  $\vec{V} = \{U, V\}$  is the velocity vector;  $U$  and  $V$  are, respectively, the velocity components in the  $X$  and  $Y$  directions;  $p$  is the pressure; and  $t$  is time. All of the above quantities are dimensionless. The conduit's half-height,  $H$ , is the length scale (i.e.,  $X = x/H$ ,  $Y = y/H$ ); the electroosmotic velocity,  $W = -\epsilon E_x(\zeta^*)_{\max}/\mu$ , is the velocity scale, and  $-\epsilon E_x(\zeta^*)_{\max}/H$  is the pressure scale. The convective time  $H/|W|$  is the time scale.  $(\zeta^*)_{\max} \neq 0$  is the maximum magnitude of the dimensional  $\zeta^*$  potential along the upper wall.  $Re = WH/\nu$  is the Reynolds number. Typically  $Re \ll 1$ .

Additionally, the incompressibility condition requires

$$\nabla \cdot \vec{V} = 0 \quad (2.2)$$

In the next section, we compute the time-independent flow field in conduits with nonuniform  $\zeta$  potential distributions.

#### ANALYTIC SOLUTION OF THE FLOW FIELD

In this section, we compute a few “characteristic” flow fields in an open conduit with nonuniform  $\zeta$  potentials along the top and bottom walls. These characteristic flow fields can serve as “building blocks” to construct more complicated flow fields. Later, we will also use these flow fields to design an electroosmotic stirrer. We assume that the embedded electrodes are adjusted in such a way as to provide a repeating (periodic) pattern with periodicity  $h$  (see Figures 1 and 2). Each cell includes  $k$  electrodes ( $k = 1, 2, 3, \dots$ ) embedded in both the conduit's bottom and top. The dimensionless length of each electrode is  $(h/k)$ . Furthermore, we assume that the gap between any adjacent electrodes is large compared to the thickness of the EDL but small compared to  $H$ . Hence, for mathematical simplicity, we can neglect the gap between adjacent electrodes. Qian and Bau<sup>16</sup> demonstrated that when the gap is relatively small ( $\ll H$ ), it has no significant effect on the flow topology. By imposing potential differences between the embedded electrodes and a reference electrode inserted in the liquid, one can control the surface charge at the solid–liquid interface and, in turn, control the concentration (and polarity) of ions in the EDL. We assume that these modulations in the charge distribution do not affect the external electric field,  $E_x$ . The field interacts with the mobile charges in the EDL to generate fluid motion. The charge polarity (positive or negative) dictates the direction of the fluid motion. To the first approximation, the velocity in the wall's vicinity can be approximated with the Helmholtz–Smoluchowski equation. Below, we denote the dimensionless slip velocity with the symbol  $U^\pm$ , where the plus and minus signs correspond, respectively, to  $Y = 1$  and  $Y = -1$ .  $U^\pm$  is assumed to be uniform along the length of the electrode, but it may vary from one electrode location to another. Consequently, our problem reduces to solving the Stokes equation with slip velocity at the walls.

(15) Probstein, R. F. *Physicochemical Hydrodynamics*; John Wiley & Sons: New York, 1994.

(16) Qian, S.; Bau, H. H. Submitted.

It is convenient to introduce the stream function,  $\Psi$ , such that  $U = \partial\Psi/\partial Y$  and  $V = -\partial\Psi/\partial X$ . The stream function satisfies the biharmonic equation

$$\nabla^4\Psi = 0 \quad (3.1)$$

with impermeable boundary conditions along a characteristic cell's boundaries,

$$\Psi(X, \pm 1) = \Psi(\pm h, Y) = 0 \quad (3.2)$$

an electroosmotic velocity distribution along the bottom ( $Y = -1$ ), and top ( $Y = 1$ ) walls,

$$\frac{\partial\Psi}{\partial Y}(X, \pm 1) = U^\pm(X) \quad (3.3)$$

and symmetry conditions at  $|X| = h$ ,

$$\frac{\partial^2\Psi}{\partial X^2}(\pm h, Y) = 0 \quad (3.4)$$

Although the biharmonic equation can be readily solved with various numerical techniques, these solutions are not sufficiently accurate for our needs later in the paper (the tracking of the motion of passive tracer particles). Therefore, we opted to use analytical techniques.

Without loss of generality, we decompose the stream function into the four components,

$$\Psi = \Psi_{EE} + \Psi_{EO} + \Psi_{OE} + \Psi_{OO} \quad (3.5)$$

where the subscripts EE, EO, OE, and OO denote, respectively, even in  $X$  and even in  $Y$ , even in  $X$  and odd in  $Y$ , odd in  $X$  and even in  $Y$ , and odd in  $X$  and odd in  $Y$ . Similarly, the boundary conditions are decomposed to

$$U_{EE}^\pm(X) = \frac{1}{4}[U^+(X) + U^+(-X) + U^-(X) + U^-(-X)] \quad (3.6)$$

$$U_{EO}^\pm(X) = \pm\frac{1}{4}[U^+(X) + U^+(-X) - U^-(X) - U^-(-X)] \quad (3.7)$$

$$U_{OE}^\pm(X) = \frac{1}{4}[U^+(X) - U^+(-X) + U^-(X) - U^-(-X)] \quad (3.8)$$

and

$$U_{OO}^\pm(X) = \pm\frac{1}{4}[U^+(X) - U^+(-X) - U^-(X) + U^-(-X)] \quad (3.9)$$

The biharmonic equation is readily solved by the method of separation of variables. Briefly, we seek a solution in the form of the Fourier series,

$$\Psi_{II}(X, Y) = \sum_{m=1}^M \frac{(-1)^m}{\alpha_m^J} x_m^J p_m^J(Y) Q_m^J(\alpha_m^J X) \quad (3.10)$$

where  $M \rightarrow \infty$ . In the above, I and J stand for either even (E) or odd (O).

$$Q_m^E(\alpha_m^E X) = \cos(\alpha_m^E X) \text{ and } \alpha_m^E = \frac{2m-1}{2h}\pi \quad (3.11)$$

$$Q_m^O(\alpha_m^O X) = \sin(\alpha_m^O X) \text{ and } \alpha_m^O = \frac{m}{h}\pi \quad (3.12)$$

The functions  $p_m^J(Y)$  are selected in such a way that the individual terms of the series (eq 3.10) satisfy the biharmonic equation, the impermeability ( $\Psi = 0$ ) condition at the boundaries, and  $\partial^2\Psi/\partial X^2(\pm h, Y) = 0$ . The coefficients  $x_m$  are computed by requiring that the tangential velocity satisfies the appropriate condition (eqs 3.6–3.9). Utilizing the orthogonality of the functions  $Q_m^J(\alpha_m^J X)$ , we find

$$x_m^J = \frac{\alpha_m^J U_m^J}{\Delta_I(\alpha_m^J)} \quad (3.13)$$

where

$$U_m^J = \frac{(-1)^m}{h} \int_{-h}^h U^\pm(X) Q_m^J(\alpha_m^J X) dX$$

and

$$\Delta_I(\xi) = \left( \frac{dp_m^J}{dY} \right)_{Y=\pm 1}$$

More specifically,

$$\Delta_E(\xi) = \frac{\xi}{\sinh^2(\xi)} - \coth(\xi) \quad (3.14)$$

and

$$\Delta_O(\xi) = -\frac{\xi}{\cosh^2(\xi)} - \tanh(\xi) \quad (3.15)$$

Witness that  $\lim_{\xi \rightarrow \infty} (\Delta_E(\xi)) = \lim_{\xi \rightarrow \infty} (\Delta_O(\xi)) = -1$ .

When the function  $U(X)$  or its derivatives are discontinuous, the rate of convergence of the series may be adversely affected (the Gibbs phenomenon). Happily, the rate of convergence can be accelerated so that only a few terms in the series are needed to achieve high precision.<sup>17,18</sup> Briefly, often the slow convergence is caused by the presence of singularities in the problem, such as a sudden change in the slip velocity at one or more locations along the wall. The presence of the singularity is reflected in the asymptotic behavior of the series coefficients. We denote  $a = \lim_{m \rightarrow \infty} x_m$  and decompose the coefficients  $x_m$  into two components:  $a$  and  $\hat{x}_m = x_m - a$ . The series associated with the coefficients  $\hat{x}_m$  typically converges rapidly and does not require any further treatment. The series associated with  $a$  is recast in

(17) Meleshko, V. V. *Proc. R. Soc. London A* **1996**, 452, 1999–2022.

(18) Meleshko, V. V.; Gomilko, A. M. *Proc. R. Soc. London A* **1997**, 453, 2139–2160.

terms of analytic functions that mimic the singularity. The resulting series converges rapidly. The methods for obtaining fast converging solutions are outlined in more detail below. Readers who are not interested in the mathematical details may skip to the section entitled Time-Independent Electroosmotic Flows.

**Even in  $X$  and Even in  $Y$  ( $\psi_{EE}$ ).** In this case,  $U^+(X) = U^-(X)$ , and the appropriate form of  $p_m^E$  is

$$p_m^E(Y) = \coth(\alpha_m^E) \frac{\sinh(\alpha_m^E Y)}{\sinh(\alpha_m^E)} - Y \frac{\cosh(\alpha_m^E Y)}{\sinh(\alpha_m^E)} \quad (3.16)$$

For brevity's sake, we drop the superscript from  $x_m$ . To accelerate the rate of convergence of the series, we decompose  $x_m$  into two components,  $x_m = a + \hat{x}_m$ , where

$$\hat{x}_m = \alpha_m^E U_m \left[ \frac{1}{\Delta_E(\alpha_m^E)} + 1 \right] \text{ and } a = -\alpha_m^E U_m \quad (3.17)$$

In the above, we removed the asymptotic ( $m \rightarrow \infty$ ) part of  $x_m$ . Consequently,  $\hat{x}_m$  decays much faster than  $x_m$ . In essence, we are decomposing the original series (eq 3.10) into the sum of two series,

$$\Psi_{EE} = \Psi_{EE}^{XY} + \Psi_{EE}^a \quad (3.18)$$

where both  $\Psi_{EE}^{XY}$  and  $\Psi_{EE}^a$  have the same form as eq 3.10, with  $\hat{x}_m$  replacing  $x_m$  in  $\Psi_{EE}^{XY}$  and  $a$  replacing  $x_m$  in  $\Psi_{EE}^a$ .

For concreteness, we consider the special case of uniform  $\zeta$  potentials along the top and bottom boundaries (i.e.,  $U^+(X) = U^-(X) = U^+$  and  $U_m = -2U^+/\alpha_m^E h$ ). Other velocity distributions can be handled in a similar way. In this special case,

$$\hat{x}_m = -\frac{2U^+}{h} \left[ \frac{1}{\Delta_E(\alpha_m^E)} + 1 \right] \text{ and } a = \frac{2U^+}{h} \quad (3.19)$$

For example, when  $h = 1$ , the first few  $x_m$  values are  $\{-1.2598, -1.0014, -1.0000, -1.0000\}$ , and the coefficients in the series (eq 3.10) decay like  $1/\alpha_m$ . In contrast, the first few  $\hat{x}_m$  values are  $\{-0.2598, -0.0014, -0.44 \times 10^{-5}, -0.11 \times 10^{-7}\}$ , and the series coefficients decay exponentially as  $m$  increases. Clearly, four terms in the  $\hat{x}_m$  series would suffice to achieve the same precision that would require the summation of hundreds of terms in the original series.

Unfortunately, our work is not yet done, because the series  $\Psi_{EE}^a$  converges slowly (like  $1/\alpha_m^E$ ). To improve matters, we expand  $p_m^E(Y)$  into the geometric series,

$$p_m^E(Y) = \sum_{v=0}^{\infty} [(2v+1-Y)e^{-\alpha_m^E(2v+1-Y)} - (2v+1+Y)e^{-\alpha_m^E(2v+1+Y)}]$$

exchange the order of summation, and sum up the resulting inner

sum in closed form to obtain<sup>19</sup>

$$\begin{aligned} \Psi_{EE}^a &= a \sum_{m=1}^{\infty} \frac{(-1)^m}{\alpha_m^E} p_m^E(Y) \cos(\alpha_m^E X) \\ &= a \sum_{v=0}^{\infty} \left\{ \sum_{m=1}^{\infty} \frac{(-1)^m}{\alpha_m^E} (2v+1-Y) e^{-\alpha_m^E(2v+1-Y)} \cos(\alpha_m^E X) - \sum_{m=1}^{\infty} \frac{(-1)^m}{\alpha_m^E} (2v+1+Y) e^{-\alpha_m^E(2v+1+Y)} \cos(\alpha_m^E X) \right\} \\ &= a \sum_{v=0}^{\infty} \{S_1(X, 2v+1-Y) - S_1(X, 2v+1+Y)\} \end{aligned} \quad (3.20)$$

where

$$S_1(\xi, \eta) = -\frac{\eta h}{\pi} \arctan \left[ \frac{\cos\left(\frac{\pi \xi}{2h}\right)}{\sinh\left(\frac{\pi \eta}{2h}\right)} \right] \quad (3.21)$$

The resulting series converges very rapidly, and it is sufficient to retain only 5 terms to obtain a relative precision better than  $10^{-5}$ . For example, when  $X = 0$ ,  $Y = 1$ , and  $h = 1$ , the first few terms in the series (eq 3.20) are  $\{5.499 \times 10^{-2}, -5.023 \times 10^{-2}, 4.447 \times 10^{-3}, -1.680 \times 10^{-5}, -9.096 \times 10^{-7}, -4.724 \times 10^{-8}, -2.384 \times 10^{-9}, -1.179 \times 10^{-10}, \dots\}$ . The series terms eventually decay faster than  $10^{-(v+2)}$ .

**Even in  $X$  and Odd in  $Y$  ( $\psi_{EO}$ ).** In this case,  $U^+(X) = -U^-(X)$ ,

$$p_m^O(Y) = \tanh(\alpha_m^E) \frac{\cosh(\alpha_m^E Y)}{\cosh(\alpha_m^E)} - Y \frac{\sinh(\alpha_m^E Y)}{\cosh(\alpha_m^E)} \quad (3.22)$$

and

$$x_m = \frac{\alpha_m^E U_m}{\Delta_O(\alpha_m^E)} \quad (3.23)$$

As before, we decompose  $x_m$  into two components.

$$x_m = a + \hat{x}_m = -\alpha_m^E U_m + \alpha_m^E U_m \left[ 1 + \frac{1}{\Delta_O(\alpha_m^E)} \right] \quad (3.24)$$

For concreteness, we consider uniform  $\zeta$  potentials along the top and bottom boundaries (i.e.,  $U^+(X) = -U^-(X) = U^+$ , and  $U_m =$

(19) Oberhettinger, F. *Fourier Expansions*; Academic: New York, 1973.

$-2U^+/\alpha_m^E h$ ). Other slip velocity distributions can be handled in a similar way. In this special case, we have

$$\hat{x}_m = -\frac{2U^+}{h} \left[ \frac{1}{\Delta_O(\alpha_m^E)} + 1 \right] \quad \text{and} \quad a = \frac{2U^+}{h} \quad (3.25)$$

We decompose  $\Psi_{EO}$  into two parts.

$$\Psi_{EO} = \Psi_{EO}^{XY} + \Psi_{EO}^a \quad (3.26)$$

In the above, both  $\Psi_{EO}^{XY}$  and  $\Psi_{EO}^a$  have the form of eq 3.10, with  $\hat{x}_m$  replacing  $x_m$  in  $\Psi_{EO}^{XY}$  and  $a$  replacing  $x_m$  in  $\Psi_{EO}^a$ .  $\hat{x}_m$  decays much faster than  $x_m$ .

Next, we expand  $p_m^O(Y)$  into the geometric series,

$$p_m^O(Y) = \sum_{v=0}^{\infty} (-1)^v [(2v+1+Y)e^{-\alpha_m^E(2v+1+Y)} + (2v+1-Y)e^{-\alpha_m^E(2v+1-Y)}]$$

exchange the order of summation, and sum up in closed form the resulting inner sum.<sup>19</sup>

$$\begin{aligned} \Psi_{EO}^a &= a \sum_{m=1}^{\infty} \frac{(-1)^m}{\alpha_m^E} p_m^O(Y) \cos(\alpha_m^E X) \\ &= a \sum_{v=0}^{\infty} (-1)^v \left\{ \sum_{m=1}^{\infty} \frac{(-1)^m}{\alpha_m^E} (2v+1+Y) e^{-\alpha_m^E(2v+1+Y)} \right. \\ &\quad \left. \cos(\alpha_m^E X) + \sum_{m=1}^{\infty} \frac{(-1)^m}{\alpha_m^E} (2v+1-Y) e^{-\alpha_m^E(2v+1-Y)} \cos(\alpha_m^E X) \right\} \\ &= a \sum_{v=0}^{\infty} (-1)^v \{ S_1(X, 2v+1+Y) + S_1(X, 2v+1-Y) \} \end{aligned} \quad (3.27)$$

The above series converges very rapidly.

**Odd in  $X$  and Odd in  $Y$  ( $\psi_{OO}$ ).** In this case,  $U^\pm(X) = -U^\pm(-X)$ ,  $U^+(X) = -U^-(X)$ ,  $p_m^O$  is given in eq 3.22 with  $\alpha_m^O$  replacing  $\alpha_m^E$  and

$$x_m = \frac{\alpha_m^O U_m}{\Delta_O(\alpha_m^O)} \quad (3.28)$$

Here we consider only the case of uniform (but different)  $\zeta$  potentials along the left ( $X < 0$ ) and right ( $X > 0$ ) halves of the upper and lower walls; i.e.,  $U^\pm(X) = -U^\pm(-X)$ , and  $U^+(X) = -U^-(X) = U^+$ . Accordingly,

$$U_m = \begin{cases} -\frac{4U^+}{\alpha_m^O h} & \text{odd } m \\ 0 & \text{even } m \end{cases} \quad (3.29)$$

Clearly, we need to consider only the odd coefficients, which we

denote with the superscript O:  $x_m^O = -4U^+/h\Delta_O(\alpha_m^O)$ . Next, we decompose  $x_m^O$  into two parts,  $x_m^O = a + \hat{x}_m^O$  where  $a = 4U^+/h$  and  $\hat{x}_m^O = -4U^+/h[1/\Delta_O(\alpha_m^O) + 1]$ . Likewise,  $\Psi_{OO}$  is decomposed into the two parts,

$$\Psi_{OO} = \Psi_{OO}^{XY} + \Psi_{OO}^a \quad (3.30)$$

where  $\Psi_{OO}^{XY}$  and  $\Psi_{OO}^a$  are formed by replacing  $x_m$  with  $\hat{x}_m^O$  and ( $a$ ) in eq 3.10. Expanding  $p_m^O(Y)$  into a geometric series, exchanging the order of summation, and summing up in closed form the resulting inner sum,<sup>19</sup> we obtain the rapidly converging series

$$\begin{aligned} \Psi_{OO}^a &= a \sum_{\text{odd } m=1}^M \frac{(-1)^m}{\alpha_m^O} p_m^O(Y) \sin(\alpha_m^O X) = \\ &a \sum_{v=0}^{\infty} (-1)^v \{ S_2(X, 2v+1-Y) + S_2(X, 2v+1+Y) \} \end{aligned} \quad (3.31)$$

where

$$S_2(\xi, \eta) = -\frac{\eta h}{2\pi} \arctan \left[ \frac{\sin\left(\frac{\pi\xi}{h}\right)}{\sinh\left(\frac{\pi\eta}{h}\right)} \right] \quad (3.32)$$

**Odd in  $X$  and Even in  $Y$  ( $\psi_{OE}$ ).** In this case,  $U^\pm(X) = -U^\pm(-X)$ ,  $U^+(X) = U^-(X)$ , and

$$x_m = \frac{\alpha_m^O U_m}{\Delta_E(\alpha_m^O)} \quad (3.33)$$

Here, we consider only the special case of uniform (but different)  $\zeta$  potentials along the left ( $X < 0$ ) and the right halves ( $X > 0$ ) parts of the upper and lower walls  $U^\pm(X) = -U^\pm(-X)$  and  $U^+(X) = U^-(X) = U^+$ . Accordingly,

$$U_m = \begin{cases} -\frac{4U^+}{\alpha_m^O h} & \text{odd } m \\ 0 & \text{even } m \end{cases} \quad (3.34)$$

As before, we decompose  $x_m^O$  into two parts,  $x_m^O = a + \hat{x}_m^O$  where

$$a = \frac{4U^+}{h} \quad \text{and} \quad \hat{x}_m^O = -\frac{4U^+}{h} \left[ \frac{1}{\Delta_E(\alpha_m^O)} + 1 \right] \quad (3.35)$$

Likewise,  $\Psi_{OE}$  is decomposed into

$$\Psi_{OE} = \Psi_{OE}^{XY} + \Psi_{OE}^a \quad (3.36)$$

The series  $\Psi_{OE}^{XY}$  and  $\Psi_{OE}^a$  are similar to eq 3.10, with  $\hat{x}_m^O$  replacing  $x_m$  in  $\Psi_{OE}^{XY}$  and  $a$  replacing  $x_m$  in  $\Psi_{OE}^a$ . Expanding  $p_m^E(Y)$  into a geometric series, exchanging the order of summation, and



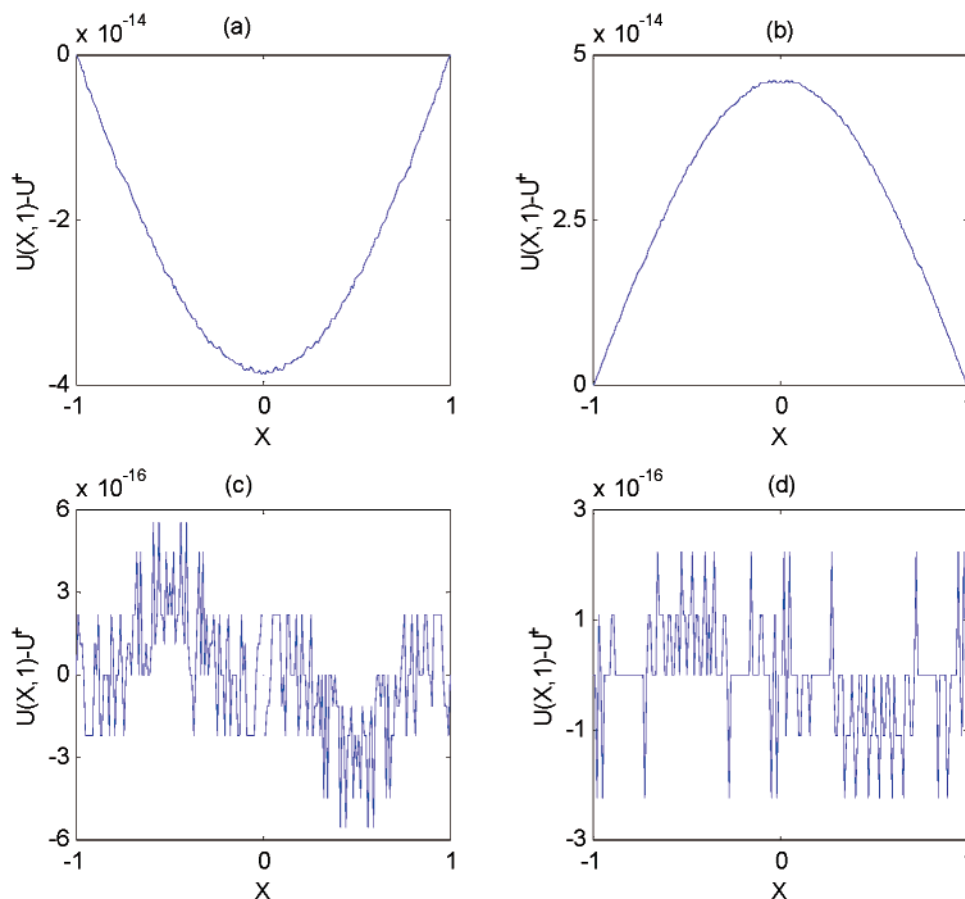


Figure 3. The difference between the velocity  $U(X, 1)$ , computed with the truncated series (10 terms), and the actual value at the boundary. (a)  $U^+(X) = U^-(X) = 1$ , (b)  $U^+(X) = -U^-(X) = 1$ , (c)  $U^\pm(X) = -U^\pm(-X)$ ,  $U^+(X) = -U^-(X)$ ,  $U^+(X) = -U^+(-X) = 1$ , and (d)  $U^\pm(X) = -U^\pm(-X)$ ,  $U^+(X) = U^-(X)$ , and  $U^+(X) = -U^+(-X) = 1$ .  $h = 1$ .

summing up in closed form the resulting inner sum,<sup>19</sup> we obtain the rapidly converging series

$$\Psi_{\text{OE}}^a = a \sum_{\text{odd } m=1}^M \frac{(-1)^m}{\alpha_m^{\text{O}}} p_m^{\text{E}}(Y) \sin(\alpha_m^{\text{O}} X) = a \sum_{v=0}^{\infty} \{S_2(X, 2v+1-Y) - S_2(X, 2v+1+Y)\} \quad (3.37)$$

**Accuracy of the Analytic Solutions.** The expressions for  $\Psi_{\text{EE}}, \Psi_{\text{EO}}, \Psi_{\text{OO}}$ , and  $\Psi_{\text{OE}}$  satisfy exactly the biharmonic equation, the impermeability ( $\Psi = 0$ ) condition at all boundaries, and the symmetry condition  $\partial^2 \Psi / \partial X^2 (\pm h, Y) = 0$ . The truncated series are required to approximate the electroosmotic velocities at the top and bottom walls. The accelerated series that we generated in this section perform this job exceptionally well and with a relatively small number of terms. As an illustration of the series' high rate of convergence, Figure 3 depicts the deviation between the actual value of the slip velocity at the boundary and the series approximation (with 10 terms) when  $h = 1$ . The boundary conditions are, respectively,  $U^+ = U^- = 1$  (3a);  $U^+ = -U^- = 1$  (3b);  $U^\pm(X) = -U^\pm(-X)$ ,  $U^+(X) = -U^-(X)$ , and  $U^+(X) = -U^+(-X) = 1$  (3c); and  $U^\pm(X) = -U^\pm(-X)$ ,  $U^+(X) = U^-(X)$ , and  $U^+(X) = -U^+(-X) = 1$  (3d). Clearly, the series solution provides an excellent approximation, even next to the singularities at  $|X| = h$  and  $X =$

0. The discrepancies between the computed values of  $U(X, 1)$  and the desired ones are smaller than  $10^{-13}$ . In the domain's interior, the precision of the analytical solution far exceeds its precision on the domain's boundaries.

#### TIME-INDEPENDENT ELECTROOSMOTIC FLOWS

The various solutions derived in the last section can be used to obtain the description of the flow field in conduits with a variety of  $\zeta$  potential distributions at their surfaces. As an example, Figure 4 depicts the four basic flow structures  $\Psi_{\text{EO}}, \Psi_{\text{EE}}, \Psi_{\text{OO}}$ , and  $\Psi_{\text{OE}}$  when  $h = 2$ . In all the computations, we used truncated series with  $M = v = 10$  terms. Figure 4a depicts equally spaced streamlines when  $U^+(X) = -U^-(X) = 1$ . The flow field consists of a single convective "cell." The flow circulates around an elliptic point (center) located at  $X = Y = 0$ . Later, we will refer to the flow pattern depicted in Figure 4a as pattern A. Figure 4b depicts the equally spaced streamlines when  $U^+(X) = U^-(X) = 1$ . In this case, the flow field consists of two counter-rotating cells with centers at  $X = 0$  and  $Y = \pm 0.58$ . The cells are separated by the surface  $Y = 0$ . Figure 4c depicts the equally spaced streamlines when  $U^\pm(X) = -U^\pm(-X)$ ,  $U^+(X) = -U^-(X)$ , and  $U^+(X) = -U^+(-X) = 1$ . Here again, the flow field consists of two counter-rotating cells separated by the surface  $X = 0$ . The centers of rotation are located at  $X = \pm 1$  and  $Y = 0$ . Finally, Figure 4d depicts the equally spaced streamlines when  $U^\pm(X) = -U^\pm(-X)$ ,  $U^+(X) = U^-(X)$ , and  $U^+(X) = -U^+(-X) = 1$ . In this case, we observe

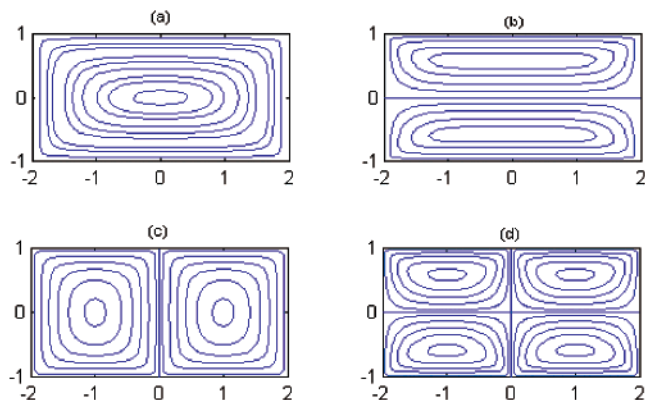


Figure 4. Streamline patterns for various electroosmotic flows when  $h = 2$ . (a)  $U^+(X) = -U^-(X) = 1$ ; (b)  $U^+(X) = U^-(X) = 1$ ; (c)  $U^\pm(X) = -U^\pm(-X)$ ,  $U^+(X) = -U^-(X)$ , and  $U^+(X) = -U^+(-X) = 1$ ; and (d)  $U^\pm(X) = -U^\pm(-X)$ ,  $U^+(X) = U^-(X)$ , and  $U^+(X) = -U^+(-X) = 1$ .

four counter-rotating cells with the surfaces  $X = 0$  and  $Y = 0$  separating the cells. Later in the paper, we will refer to the flow pattern depicted in Figure 4d as pattern B. The various patterns depicted in Figure 4 can be superimposed (with various weighing factors) to generate additional flow topologies.

The figures illustrate that it is possible to generate complex flow patterns when the distribution of  $\zeta$  potentials along the conduit's walls is not uniform. Witness that the flow has a velocity component transverse to the conduit's axis. Such flow patterns may assist in moving material from one side of the conduit to the other and, thus, assist in stirring. The flow is, however, highly regular, and in the absence of diffusion, passive tracer particles will follow the streamlines without any transport transverse to the streamlines. Thus, the types of flows illustrated in Figure 4 are not likely to make good stirrers. To obtain better stirring, it would be desirable to have tracer particles spread all over the conduit. This objective can be achieved with chaotic advection, which we discuss in the next section.

#### CHAOTIC ADVECTION INDUCED BY ELECTROOSMOSIS

In this section, we demonstrate that with appropriate temporal modulation of the  $\zeta$  potential, one can induce chaotic advection. The basic idea is quite simple. We alternate between two or more flow patterns. For example, we refer to the flow patterns depicted in Figure 4a,d as patterns A and B, respectively. We maintain the flow field A for the time interval  $0 < t < T/2$ , switch to the flow field B for the time interval  $T/2 < t < T$ , and then switch back to flow A. The process is repeated with a period  $T$ . The switching from one flow pattern to another is accomplished by controlling the distribution of the  $\zeta$  potential with the aid of the embedded electrodes (Figures 1 and 2). It is easy to imagine the trajectory of a passive (nondiffusing) tracer particle. In the time interval  $0 < t < T/2$ , the particle will follow the streamlines that correspond to flow pattern A. In the time interval  $T/2 < t < T$ , the particle will follow the streamlines that correspond to pattern B. As the flow field alternates between A and B, the particle will trace a zigzag path that eventually will cause it to sample most of the conduit's area. This is the type of behavior that one would desire in an efficient stirrer.

To describe the above chain of events quantitatively, we assume that the Reynolds number is small and inertial effects can

be neglected. The period  $T$  of the alternations in the  $\zeta$  potential is large enough that the flow is quasistatic, and the instantaneous flow fields are given by the steady-state solutions of the Stokes equations. Finally, we assume that the equilibration time constant of the double layer is much smaller than  $T$ . Many of these assumptions have been widely used when studying mixing problems at low Reynolds numbers.<sup>14,20–22</sup>

When the flow field alternates between patterns A and B, the instantaneous flow field is given by

$$\Psi(X, Y, t) = f_A(t)\Psi_A(X, Y) + f_B(t)\Psi_B(X, Y) \quad (5.1)$$

where subscripts A and B correspond, respectively, to flow patterns A and B. In the above,

$$f_A(t) = \begin{cases} 1 & kT < t < kT + \frac{T}{2} \\ 0 & kT + \frac{T}{2} < t < (k+1)T \end{cases} \quad (5.2)$$

and

$$f_B(t) = \begin{cases} 0 & kT < t < kT + \frac{T}{2} \\ 1 & kT + \frac{T}{2} < t < (k+1)T \end{cases} \quad (5.3)$$

where  $k = 0, 1, 2, \dots$  is an integer, and the resulting flow field is periodic in time, with a periodicity  $T$ .

The “on–off” nature of eqs 5.2 and 5.3 is not quite consistent with the Stokes approximation that requires the time constant associated with the modulations to be larger than the viscous time constant. Aref and Balachandar<sup>20</sup> have, however, investigated the effects of various protocols on the kinematics of the flow between two alternately rotating eccentric cylinders and determined that an “on–off” protocol gives qualitatively indistinguishable results when compared to ones obtained with “smoother” protocols. Indeed, a function  $f(t)$  that provides a more gradual time-wise change will modify only the “effective” time interval  $T_i$  without changing the qualitative nature of the flow. Finally, we note that the more interesting flow phenomena occur when  $T$  is relatively large and when the quasistatic approximation is likely to be valid.

The motion of a passive tracer can be computed by solving the kinematic equations

$$\left. \begin{aligned} \frac{dX}{dt} &= f_A(t)\frac{\partial\Psi_A(X, Y)}{\partial Y} + f_B(t)\frac{\partial\Psi_B(X, Y)}{\partial Y} \\ \frac{dY}{dt} &= -f_A(t)\frac{\partial\Psi_A(X, Y)}{\partial X} - f_B(t)\frac{\partial\Psi_B(X, Y)}{\partial X} \end{aligned} \right\} \quad (5.4)$$

with the initial conditions

$$X(0) = X_0, \quad Y(0) = Y_0 \quad (5.5)$$

(20) Aref, H.; Balachandar, S. *Phys. Fluids* **1986**, *29*, 3515–3521.

(21) Chaiken, J.; Chu, C. K.; Tabor, M.; Tan, Q. M. *Phys. Fluids* **1987**, *30*, 687–694.

(22) Yi, M.; Qian, S.; Bau, H. H. *J. Fluid Mech.*, in press.



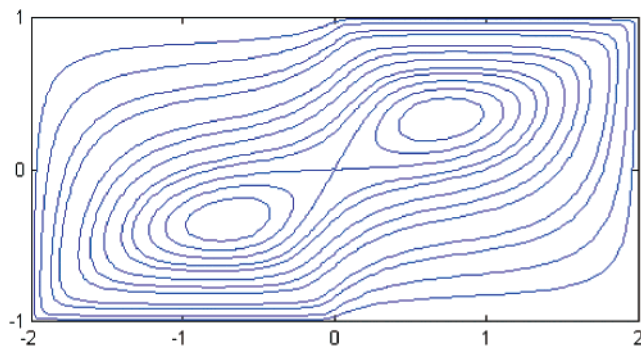


Figure 5. Streamline pattern for the superimposed flow structure AB when  $h = 2$ . The individual patterns A and B are depicted, respectively, in Figure 4a,d.

We compute the particle's trajectory by integrating eq 5.4 using the fourth-order Runge–Kutta algorithm.

Often, stroboscopic images (Poincaré sections) are used to study the stirring process. These images are obtained by integrating the kinematic equations and documenting the tracer particle's location at the end of each period. In other words, each image is a superposition of snapshots that depict the location of the tracer particle at times  $t = kT$ , where  $k = 0, 1, 2, \dots$ . When the pattern of points lies on a smooth curve, the motion is deemed to be regular and provides poor stirring. When a scattered pattern emerges, the motion is likely to be chaotic.

Here we will alternate between patterns A and B and study the flow patterns as  $T$  increases. Although the expression (5.4) is valid for a relatively large  $T$ , it is instructive to examine the flow field when the alternation's frequency is high, that is, in the limit of  $T \rightarrow 0$ . The flow patterns in this limit are depicted in Figure 5, and they consist of the superposition of patterns A and B. When  $T = 0$ , the system (5.4) is autonomous and integrable. As already noted by Aref<sup>44</sup> among others, the equations (5.4) are a Hamiltonian system. The flow conserves area, and the phase space  $(x, y)$  coincides with the physical space. The phase space portrait (Figure 5) is reminiscent of a phase space of a nonlinear oscillator, and it consists of elliptic fixed points surrounded by closed orbits (tori) of periods ( $\Gamma$ ) ranging from 0 to infinity. The two families of periodic orbits are separated with homoclinic orbits that pass through a hyperbolic (saddle) point.

When  $T$  is small but larger than zero, the system may no longer be integrable. Chaotic behavior may arise because of both the disruption of the hyperbolic fixed point and the perturbation of the tori. In the first instance, the stable and unstable manifolds of the hyperbolic point (in the Poincaré section) will intersect transversely infinitely many times to form a homoclinic tangle and a "hyperbolic mixing region." Additionally, according to the Poincaré–Birkhoff theorem,<sup>23</sup> the tori with rational period ratios ( $\Gamma/T$ ) will deform significantly and form a "petal" structure that leads in the Poincaré section to the formation of a sequence of new hyperbolic (saddle) and elliptic fixed points. Like the original hyperbolic point, these newly formed hyperbolic points will give rise to chaotic behavior. In contrast, according to the Kolmogorov–Arnold–Moser (KAM) theorem, most of the tori with irrational period ratios will distort only slightly and separate

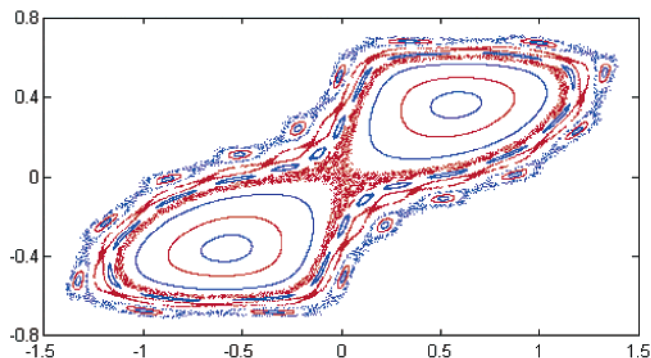


Figure 6. Poincaré section when  $T = 1.6$  and  $h = 2$ . Passive tracer particles were initially placed at  $(-1,0)$ ,  $(-0.9,0)$ ,  $(-0.85,0)$ ,  $(-0.65,0)$ ,  $(-0.5,0)$ ,  $(-0.3,0)$ ,  $(-0.25,-0.1)$ ,  $(-0.5,-0.2)$ ,  $(-0.6,-0.3)$ ,  $(0.25,0.1)$ ,  $(0.5,0.2)$ , and  $(0.6,0.3)$ .

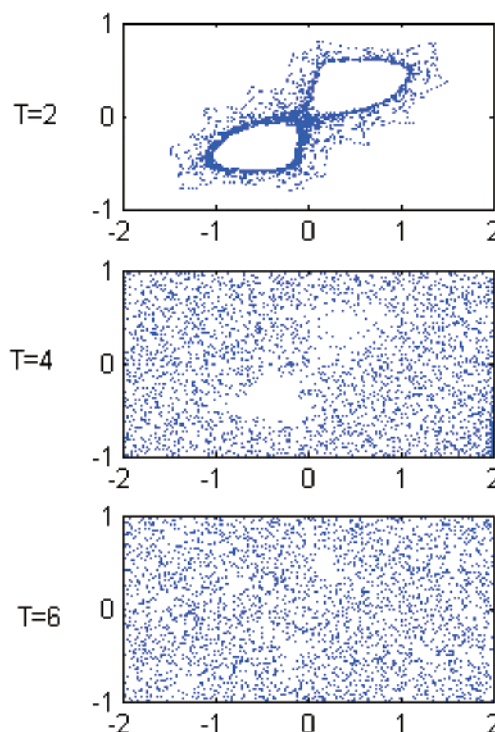


Figure 7. Poincaré sections for various periods  $T = 2, 4$ , and  $6$ .  $h = 2$ . A passive tracer particle was initially inserted at  $(x_0, y_0) = (0, 0.01)$ , and its motions were followed for 3000 periods.

between the regions of irregular behavior. This process is illustrated in Figure 6. The figure depicts the stroboscopic image (Poincaré section) of the passive tracer particles' trajectories when  $T = 1.6$  and  $h = 2$ . The "particles" were initially inserted at locations:  $(-1,0)$ ,  $(-0.9,0)$ ,  $(-0.85,0)$ ,  $(-0.65,0)$ ,  $(-0.5,0)$ ,  $(-0.3,0)$ ,  $(-0.25,-0.1)$ ,  $(-0.5,-0.2)$ ,  $(-0.6,-0.3)$ ,  $(0.25,0.1)$ ,  $(0.5,0.2)$ , and  $(0.6,0.3)$ . Witness the emergence of a chaotic region resulting from the homoclinic tangle and the formation of new hyperbolic and elliptic points.

As  $T$  increases, so does the complexity of the flow. Figure 7 depicts the Poincaré sections of a particle's trajectory when  $T = 2, 4$ , and  $6$ . The particle was initially inserted at  $(0, 0.01)$ , and its motion was followed for 3000 periods. When the period  $T$  is small ( $T = 2$ ), the particle wanders around the superimposed streamlines of Figure 5. As the period  $T$  increases, it strays further away from the "regular path" and samples most of the cell's area. This

(23) Ottino, J. M. *The Kinematics of Mixing: Stretching, Chaos, and Transport*; Cambridge University Press: New York, 1989.

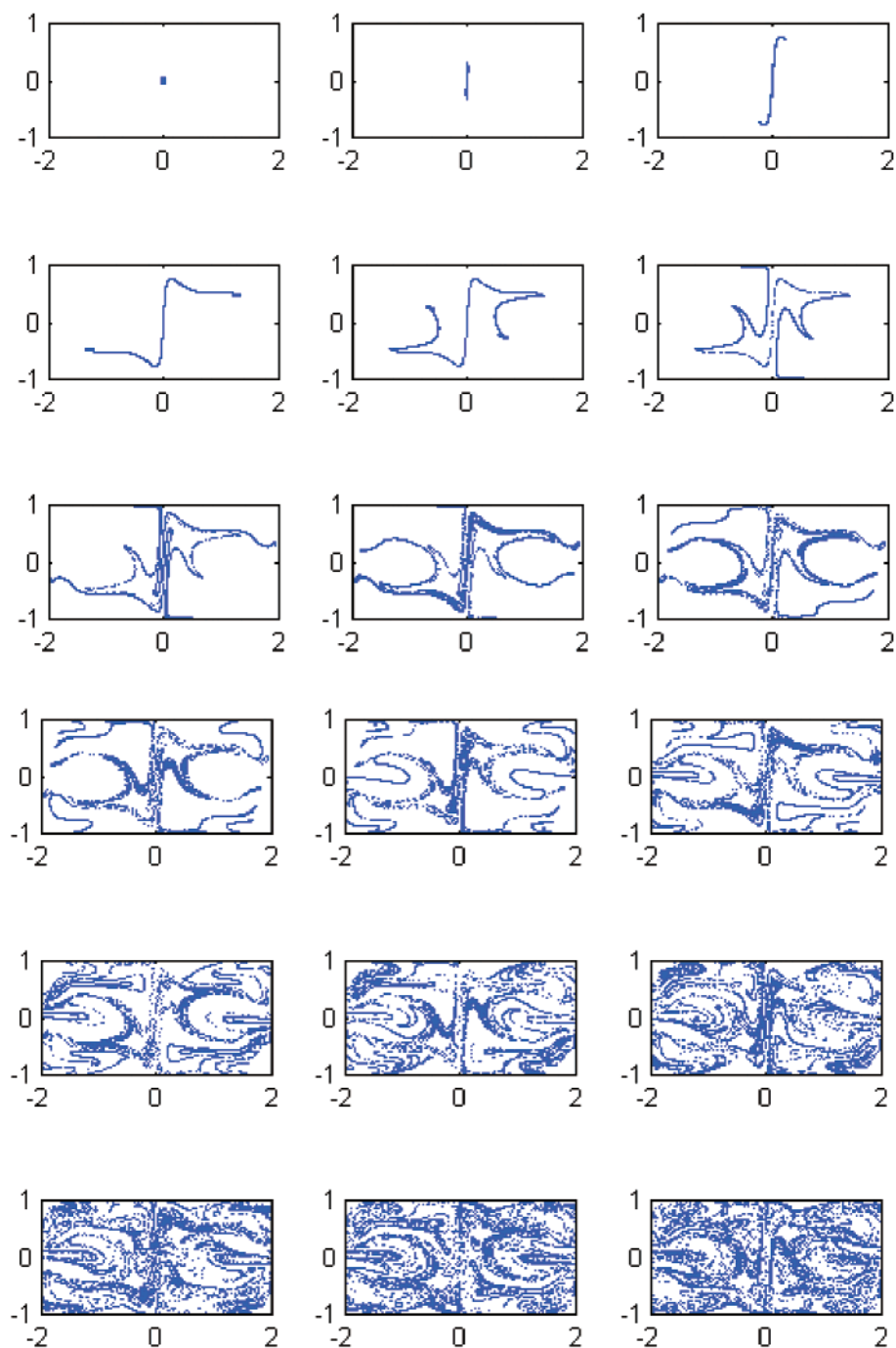


Figure 8. Deformation of a blob with an initial edge size of 0.1, initially ( $t = 0$ ) centered at (0,0).  $T = 4$ .  $t/T = 0, 1, \dots, 17$ .

indicates efficient stirring within the single cell. Witness the presence of exclusion zones when  $T = 4$ . The size of these exclusion zones decreases as  $T$  increases ( $T = 6$ ).

To better describe the stirring process, like Aref,<sup>14</sup> we inserted in the conduit a square material blob of edge size 0.1 initially centered at (0, 0). The experimental analogue of the blob is a drop of dye inserted into the conduit. We tracked the deformation of this material blob by tracking the trajectories of  $10^4$  particles, initially evenly distributed within this square. When  $T = 4$ , Figure 8 depicts the Poincaré sections at times 0,  $T$ ,  $2T$ , ..., and  $17T$ . Witness the rapid stretching and folding process that is characteristic of chaotic advection. Eventually, the blob has spread to

cover the entire cell's area. Such behavior is desired in an efficient stirrer.

In the above, we described the case when the dimensionless length of the electrodes is 1 and  $h = 2$ . In other words, the representative cell contains two embedded electrodes in each wall. The size of the mixing region is, therefore, of length 2, and there is no mass transport between adjacent cells. One has, however, a great amount of flexibility in selecting the size of the mixing region. For example, one can extend the mixing region by selecting a larger value for  $h$ . Figure 9a–c depicts, respectively, the flow patterns A and B (with  $h = 4$ , i.e., the representative cell contains four embedded electrodes in each wall), and the

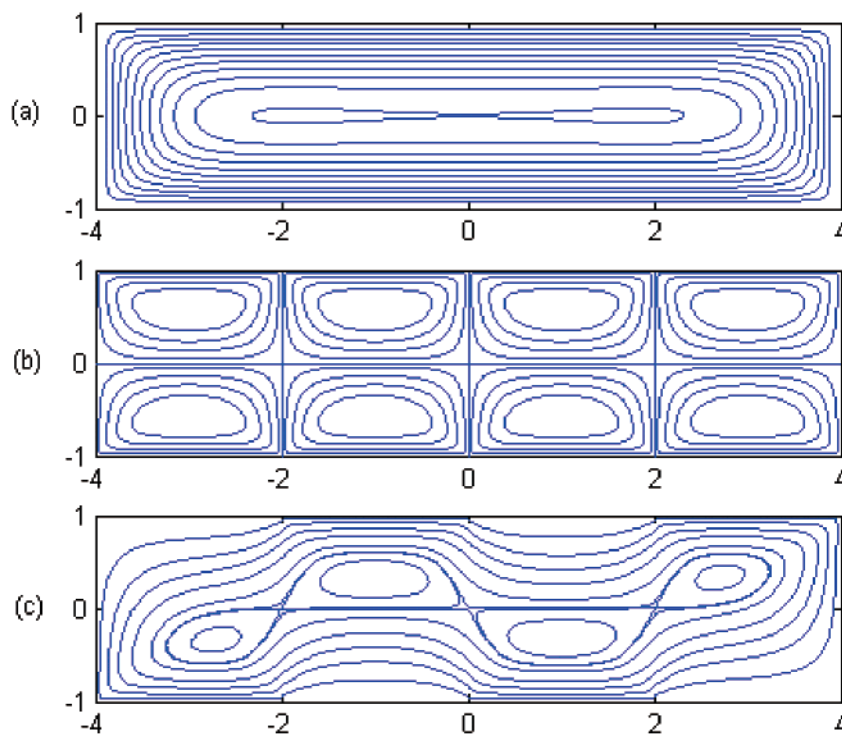


Figure 9. Streamline pattern A when  $h = 4$  (a), streamline pattern B when  $h = 2$  (b), and the superposition AB (c).

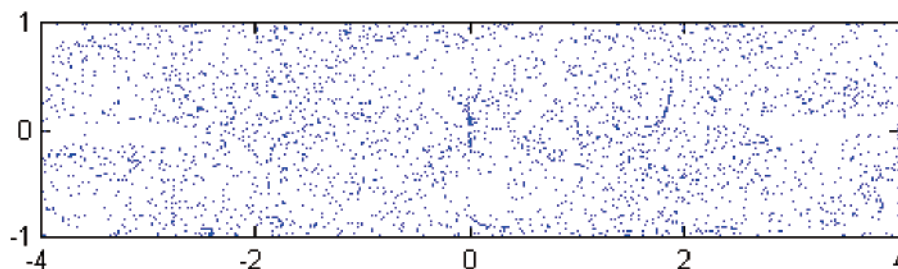


Figure 10. Poincaré section when  $T = 4$ . The passive tracer particle was initially inserted at  $(x_0, y_0) = (2, 0)$  and followed for 3000 periods.

superimposed flow fields. When  $T = 4$ , Figure 10 depicts the stroboscopic images (Poincaré section) of a passive tracer particle initially inserted at  $(x_0, y_0) = (2, 0)$ . The particle was followed for 3000 periods. Witness that eventually the particle sampled the conduit section  $-4 < X < 4$ . This can be contrasted with Figure 7, in which the passive tracer particles sample the smaller region  $-2 < X < 2$ .

Although the flow patterns A and B alone are both periodic in  $x$ , it is also possible to control the electrode potentials so that the alternating field  $A + B$  is not periodic, and passive tracer particles are not confined to specific regions in the conduit.

## CONCLUSIONS

In this paper, we studied electroosmotic flows in a conduit with nonuniform  $\zeta$  potentials along its walls. The nonuniformity of the  $\zeta$  potentials induces complex flow patterns in the conduit. The flow field was computed accurately with the aid of accelerated Fourier series. The truncated Fourier series provided accurate descriptions of the flow fields with just a few terms. Such high precision is essential in order to enable one to track the motion of passive tracer particles over many periods. The various analytic solutions that we obtained here can be used as building blocks to obtain other flow patterns with the method of superposition.

By appropriate time modulation of the  $\zeta$  potential, one can alternate among two or more flow patterns and induce chaotic advection and efficient stirring in the conduit. There are many choices for possible flow patterns. The selection of combinations that lead to the most efficient stirring process is an interesting optimization problem that we do not address here.

The electroosmotic stirrers may be particularly beneficial for microfluidic systems. In microfluidic systems, it is difficult to incorporate moving components, and turbulence is not available to stir the fluid. Hence, mixing is a challenge. This paper outlines a concept that can allow one to design microfluidic mixers that utilize chaotic advection and do not require any moving components.

## ACKNOWLEDGMENT

The work described in this paper was supported, in part, by DARPA (Dr. Anantha Krishnan, Program Director) through a grant to the University of Pennsylvania.

Received for review February 27, 2002. Accepted May 9, 2002.

AC025601I